In situ measurements of the crossing vibrations of a railway turnout

Boogaard, M. A.; Li, Z.; Dollevoet, R. P.B.J.

DOI
10.1016/j.measurement.2018.04.094

Publication date
2018

Document Version
Final published version

Published in
Measurement: Journal of the International Measurement Confederation

Citation (APA)
Boogaard, M. A., Li, Z., & Dollevoet, R. P. B. J. (2018). In situ measurements of the crossing vibrations of a railway turnout. *Measurement: Journal of the International Measurement Confederation*, *125*, 313-324. https://doi.org/10.1016/j.measurement.2018.04.094

Measurement 125 (2018) 313–324

Contents lists available at ScienceDirect

Measurement

journal homepage: www.elsevier.com/locate/measurement

In situ measurements of the crossing vibrations of a railway turnout

M.A. Boogaard, Z. Li[*], R.P.B.J. Dollevoet

Railway Engineering, Faculty of Civil Engineering and Geosciences, Delft University of Technology, Stevinweg 1, 2628 CN Delft, The Netherlands

ARTICLE INFO

Keywords:
Railway crossings
Railway turnout
Pass-by measurement
Condition monitoring
Output only measurement

ABSTRACT

Vibration-based condition monitoring is a powerful tool for remotely assessing the quality of railway components. Due to its design, railway crossings suffer from faster degradation, because of the transition from stock rail onto the needle. Since this is also a repetitive load, a small amount of wear will increase the degradation. Measuring the dynamic response also contains information about the transition of the train wheel from the stock rail onto the needle.

In this paper, a setup that measures the acceleration and the strain of a railway crossing during train passages is presented. The responses of these two measurement techniques are analyzed for two different types of trains. A linear correlation between the peak values of the strain and the nominal axle load is presented with a regression value of $-1.8 \cdot 10^{-5}$. From the accelerations, both the displacement and the transient wheel-rail contact can be analyzed.

1. Introduction

Railway turnouts provide flexibility for train operation and allow for a more efficient use of the railway network. Compared to straight track, railway turnouts require a more complex structure that typically deteriorates faster. Moreover, failure of a turnout causes considerable disruption for the train operator.

There are two sections of the turnout that suffer from fast degradation: the switch blades and the crossing. The switch blades are the movable track components that determine whether a train takes the straight or diverging route through the turnout. Because of the lateral forces, this section suffers from a substantial amount of wear.

The region where the straight and diverging routes intersect is called the crossing or the frog, and this region is the focus of this paper. Because of the design of train wheels, there has to be a gap to allow the flange to pass through the crossing in each direction. A frog suffers from both high wear and impact loading due to the change in wheel-rail contact. This contact is very complex because of its transient nature and the transition from the stock rail onto the needle; therefore, this contact is an active field of research. Furthermore, the dynamic stiffness is different compared to plain track and varies along the length of the frog, which also has a considerable influence on the train-track interaction.

Due to the high dynamic loading, vibration-based condition monitoring can be very suitable for these components. Ideally, this monitoring should be performed by a train-borne measurement, which has already been successfully tested for the early detection of squats [1] and also presented by [2]. To further enhance these measurements and to verify the train-borne measurements, ground measurements are needed. In this paper, a measurement setup to monitor the dynamic response of a frog caused by passing trains is presented.

In the next section, the background, aim and scope of this paper are presented. In Section 3, the design of the measurement setup is shown, and in Section 4, the measurement results are presented, including a comparison between two different types of trains. In Section 5, a more detailed analysis of these data is performed, and in Section 6, the findings and implications are discussed.

2. Literature review and scope

There are many publications that deal with high frequency wheel-rail interaction, like [3] and also studies that focus on the transient wheel-rail contact in crossings, such as [4,5], but the majority of these publications only contain numerical simulation results. Although these results have already provided considerable insight into the transient contact, field work is needed to verify the results obtained through simulations. In this section, a brief overview of the literature containing field work will be presented.

Extensive overviews of wayside track monitoring are available in [6,7]. The focus in [6] is to detect the quality of the rolling stock by installing different types of sensors in a straight track. These authors concluded that accelerometers and strain gauges are effective for monitoring wheel impacts caused by wheel imperfections. Strain gauges can also be used to determine the loading with weighing-in-

---

[*] Corresponding author.
E-mail addresses: m.a.boogaard@tudelft.nl (M.A. Boogaard), z.li@tudelft.nl (Z. Li).

https://doi.org/10.1016/j.measurement.2018.04.094
Received 2 August 2017; Received in revised form 26 April 2018; Accepted 28 April 2018

motion techniques.

A more focused review is available in [7]. Their objective is to measure the dynamic deflection of the rail to derive dynamic characteristics, such as the speed of the vehicle, as well as wheel-rail interaction forces and track deformation. These authors concluded that a combination of strain gauges and accelerometers would be very interesting for the condition monitoring of a railway infrastructure. Regarding the strain gauges, these authors favored the use of optical sensors.

A remote network for condition monitoring was presented by Liu Chong et al. [8]. This network was based on data acquisition nodes that are attached to the rail, where each node measures the vertical acceleration and vertical strain simultaneously using a single transducer for each quantity. The sampling frequency for the strain was limited to 1 kHz, and the accelerometers were sampled at 5 kHz. Although a successful field test was performed, no data analysis was conducted in this paper.

The above papers are limited to plain track. One of the first articles to present the train-track interaction for a railway crossing together with a validation measurement was by Kassa and Nielsen [9]. In this work, the authors used strain gauges attached to the wheels to measure the contact forces. Although this is a commonly used approach for obtaining the contact force, this method relies on a proper dynamic calibration. With this method, insights into the loading condition are obtained, but no direct data are obtained from the response of the crossing itself.

A similar approach for measuring the contact forces in the crossing was presented by Nicklisch et al. [10]. In this paper, a setup was used that consists of strain gauges attached to the frog. This arrangement was based on the *static* assumption that the impact force is equal to the summation of the forces at the boundary of the section in which the impact occurs. Two sets of strain gauges were used. The first set was used to measure the shear strain before and after the region where the frog is impacted. The second set was used to measure the strain in the rail foot above the sleepers. This setup was calibrated in a lab environment before being installed in the field.

Another paper is that by Bruni et al. [11], where the accelerations of an urban turnout caused by the passing of a metro were measured and presented, but no details were provided about the measurement itself. In this work, it was assumed that the vibrations of the crossing nose were measured using an accelerometer. These results were low-pass filtered at 500 Hz.

A system called Automated Point Inspection (API)[1] was developed by Witt Industrial Electronics from Germany together with Deutsche Bahn [12]. This setup consists of an axle counter that needs to be installed in front of the frog and a 3D accelerometer that can be attached anywhere on the frog. Additionally, this setup can be equipped with an accelerometer, which is integrated twice to assess the sleeper displacement. This system can sample up to 10 kHz. Based on this measurement, the location of impact and the relative magnitude can be estimated.

This overview presents some promising results for condition monitoring. It is shown that accelerometers and strain gauges can be successfully used to monitor plain track; however, work in which a similar setup is used for special track components is limited. In this paper, an approach will be presented for railway crossings. This study will highlight some practical aspects. A major contribution of this paper is presenting the measurement data with more detail such that other researchers in this field can relate their study to this field work. The long-term goal of the work presented herein is to perform vibration-based condition monitoring on rail components.

Apart from practical issues, there are also two other hurdles to overcome. The first hurdle is politics. Generally, there is a two-layer structure for track operations. There is an infrastructure manager who ensures that the track is available for the train operators, and there are contractors who perform the actual field maintenance. Both need to collaborate to perform field tests, particularly in a longer term, but in everyday life, the infrastructure manager is a customer of the contractor. The second hurdle is related to safety. Not only should this research have no influence on train operation but there are also safety rules that must be followed, and these rules state that it is not possible to be on the track during normal operation.

3. Description of measurement setup

The proposed setup is designed to capture the short wave dynamics of a frog caused by the impact of passing trains. Given that the railway track is a nearly infinite structure, the aim is to obtain a measure on how the frog is impacted by the train and its response.

Regarding sensor selection, it is very common to measure acceleration because this is an absolute measurement. It is also possible to measure velocity or displacement, although each quantity has its own benefits. Whereas displacement is the easiest quantity to interpret, it poses some practical problems. For instance, a displacement measurement always needs a fixed reference point, which makes accelerometers the preferred sensor.

Railways are expected to have high levels of electromagnetic noise and are also a quite harsh environment. Therefore, industrial-grade sensors were sourced. These sensors have internal electronics that handle the signal conditioning based on the IEPE principle; thus, disturbance from the train is kept to a minimum. Since the magnitude of the accelerations was not known beforehand, sensors with a dynamic range of 500 g were selected, namely, the 603C00 sensors from IMI. These sensors are not the smallest or lightest sensors available, but compared to the object of interest, the weight of the sensor is not expected to have any influence on the dynamics. Additionally, these sensors are relatively inexpensive, thus making them even more suitable for use as disposable items. The relevant specifications of these sensors are presented in Table 1.

Another option is to use strain gauges. A number of different mounting options are available for strain gauges, which all have their own benefits. Most often, strain gauges are placed on the rail web and can measure vertical and/or lateral deformation, depending on the configuration and orientation. Strain gauges can also be placed on the rail foot to measure the deformation in the longitudinal direction.

In [13], it was shown that strain gauges can be used to measure surface waves caused by impact. Furthermore, since strain gauges can be very compact, they can be installed close to the location of the impact.

There are basically two types of strain sensors: those based on optical fibers and those based on resistive foil. Optical strain gauges are relatively new and provide many advantages. Because light is used to transport the information, these sensors are immune to electromagnetic interference, and extremely long cables can be used. Furthermore, multiple sensors can be built in a single fiber, which improves the ease of installation. This advantage of course comes with a cost increase, both for the sensors and the signal conditioner.

Resistive foil strain gauges are the conventional sensors typically used for strain measurements. These measurements are based on a small change in resistance, thus making the measurements susceptible to noise. Furthermore, good quality cables are required, which should be kept as short as possible. A more in-depth comparison between the different types of strain gauges and their applicability to railway applications can be found in [7].

Due to the cost advantage, resistive foil strain gauges were used. The sensors selected for this measurement are single, linear, waterproof and made by Kyowa. These gauges were used in quarter bridge configuration and AC coupled to remove static deviations. Further details of the

---

[1] In German, this system is called Elektronische SystemAnalyse Herzstückbereich (ESAH).

Table 1

Technical specifications of the selected accelerometer, type 603C00 from IMI.

Model	603C00
Sensitivity	10 mV/g
Measurement range	500 g
Frequency range (±3 dB)	0.5–10 kHz
Resolution	2000 µg
Spectral noise (1 kHz)	$5\,\mu g/\sqrt{Hz}$
Weight	51 g
Height	42.2 mm

Table 2

Technical specifications of the selected waterproof foil strain gauges from Kyowa.

Model	KFW-5-120-C1-11
Resistive element material	CuNi alloy foil
Operating temperature range	− 10 to 80 °C
Strain limit	2.8 (%)
Gauge factor	2.1 (–)
Resistance	120 Ω
Grid length	5 mm
Grid width	2 mm

strain gauges used in this work are presented in Table 2.

The strain gauges were not calibrated after the installation, so the measured strains presented in this publication are the changes of the impedance from the strain gauge in quarter bridge configuration. These are proportional to the strain and can be converted to actual strain by multiplying the impedance chance by the gauge factor.

The largest deformation is expected from the needle. Because these sensors will be installed on the crossing in the field, gluing the sensors to the side of the needle to resemble the rail-web-mounted orientation is not possible. However, there is a flat horizontal surface to the side of the needle where the strain gauges can be attached. In this way, the deformation in the longitudinal direction can be measured. An overview of the designed sensor layout is shown in Fig. 1.

Consistent with the results of [13], the strain gauges were located around the location of the impact and slightly farther away in an attempt to capture the surface waves. The strain gauges were glued to a milled surface, which is relatively well defined. The final installation is shown in Fig. 2.

The accelerometers were expected to be better suited to measure the more global behavior of the frog; thus, they were placed farther from the impact. The accelerometers were screwed to a PVC bracket, which was glued to the side of the frog at the indicated locations. Each of these sensors was connected to a shielded twisted-pair cable. A close-up view of how these sensors were attached is presented in Fig. 2. From this photo, the robust design of the sensor is also clear.

To collect the data, a PAK MKII data acquisition system from MuellerBBM was used, which also handles the signal conditioning of both types of sensors. The data acquisition was performed from a safe location at the side of the track, and for this purpose, the cables were extended by approximately 30 meters. The transient wheel-rail contact is expected to have a wavelength of approximately 3 ms or even shorter, which requires a sampling rate of at least 10 kHz. The sampling frequency was set to 102.4 kHz, which is the highest sampling rate possible for the current configuration.

For the first field installation, a frog near Amsterdam Central Station was selected. This frog is quite heavily used, mainly in the straight-through direction with the impact on the needle. On average, over 100,000 axles per month pass over this frog in the straight-through direction, with a total load of 1.4 megatonnes. These are mainly (international) passenger trains but also include a small amount of freight trains. Because this frog is located close to the station, the velocity of the train is limited to 40 km/h.

4. Measurement results

The measurement data are presented in this section. From the different train types that are recorded, two distinct train types are selected for this work. These two train types were selected because they have very different physical properties. First, these properties will be described, and then the raw data are presented. In Section 4.2, the raw data are compared.

The first train type is an international passenger train known as IntercityDirect (ICD). This train is composed of an electric locomotive (TRAXX) at the front and a variable number of ICR-type passenger coaches. The average axle load for the TRAXX locomotive is 21 tonnes, and the axle load for an ICR passenger wagon is 11.7 tonnes. This type of train is typically only used for a small section of the network.

The second type of train is a double-decker train, also known as a VIRM type of train. This type of train is an electric multiple unit (EMU), which uses self-propelled passenger coaches. This train comes in two compositions with either four or six coaches. These two compositions can also be combined arbitrarily. For the VIRM train with four coaches, traction is provided by the first and last coaches. These coaches have an average axle load of 16.8 tonnes, and the average axle load for the non-driven coaches is 14.2 tonnes. This is a very commonly used type of train throughout the Netherlands.

A full time history of the passage of a VIRM train with four coaches is shown in Fig. 3. The responses of only three sensors are shown for clarity. For every coach, there are two sets of peaks, which result from the passage of the bogies. Additionally, every bogie comprises of two large peaks, which are the passages of the wheels through the crossing.

From Fig. 4, large peaks from the passage of the axles are clearly identified. Based on the time between the peaks and the axle spacing, the speed of this train is initially slightly higher than 11 m/s, which is the maximum allowed speed at this location, and the train is decelerating. The large acceleration peaks are preceded and followed by lower peaks. These peaks are caused by the axles running over the thermite welds at both ends of the frog. Furthermore, note that the magnitude of the accelerations is very small between the bogies of each coach. The ICD-type train exhibits a very similar time history.

When zooming in on one of the passages, the obtained response is as shown in Fig. 4. In this case, the passage of the tenth axle of the VIRM train from Fig. 3 is shown.

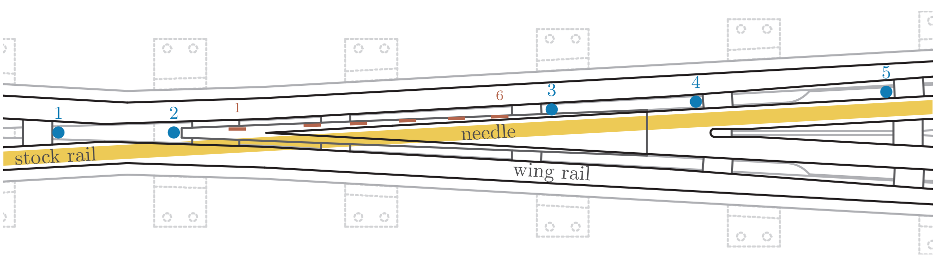

Fig. 1. Designed sensor layout on a 1:9 constructed frog. The locations of the accelerometers are indicated with the blue dots and numbers. The red lines indicate the locations of the strain gauges. For clarity, only the first and last strain gauges are numbered. A straight approximation of the trajectory of the wheels through this crossing in the main direction is highlighted by the yellow line. (For interpretation of the references to colour in this figure legend, the reader is referred to the web version of this article.)

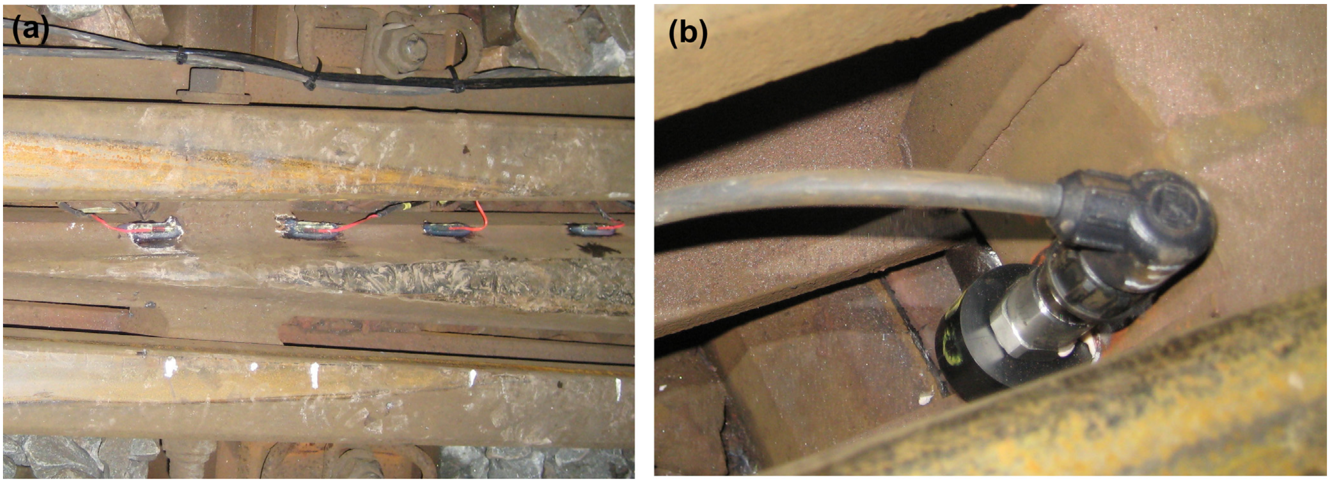

Fig. 2. (a) In this photo, four strain gauges can be observed. They are attached to a flat surface 50 mm below the running band of the train. This photo also shows the transition from the stock rail onto the needle. (b) This photo shows how the accelerometers are attached to the frog. The black PVC ring at the bottom has a flat side, which is glued to the frog. The accelerometer is then attached with a stud to this ring.

From Fig. 4, it is clear that the accelerations have a considerably shorter wavelength compared to the strain measurement, which is why different scales are used for the time axis. The top plot shows the raw, unfiltered signal, but measuring strain is much more difficult. The original signals contain substantial noise; therefore, the results shown here are bandpass filtered. Wavelet transformation is used to design a bandpass filter where all frequency content between 1 and 500 Hz is kept, and the remaining content is fully attenuated. The upper limit of 500 Hz is tuned to minimize the noise while keeping the instantaneous response just after t = 0.

When examining the different sensor locations, a couple of observations are apparent. The response of accelerometer 1 is smaller and shows a longer wavelength compared to the other four sensors. As shown in Fig. 1, accelerometer 1 is attached to a spacer. Thus, the vibrations with a shorter wavelength will not be transmitted through the bolt connections. This sensor only follows the more global behavior of the crossing.

Furthermore, it is observed that the crossing exhibits a traveling wave behavior. Based on the running band of the wheel over the frog, the transition from the stock rail onto the needle occurs between accelerometers 2 and 3. The responses of these sensors are mostly in phase. The responses of sensors 4 and 5, which are located farther from the impact, show a delay with respect to those of sensors 2 and 3. Based on the cross correlation between sensors 3 and 4, a wave speed of nearly 1800 m/s is found.

Sensor 2 shows the largest amplitude for the transition from the stock rail onto the needle. Approximately 2 ms later, a second peak appears. The wavelength of the second peak also appears to be shorter compared to that of the first peak. Given the speed of this train, the distance traveled by the train between these two instances is

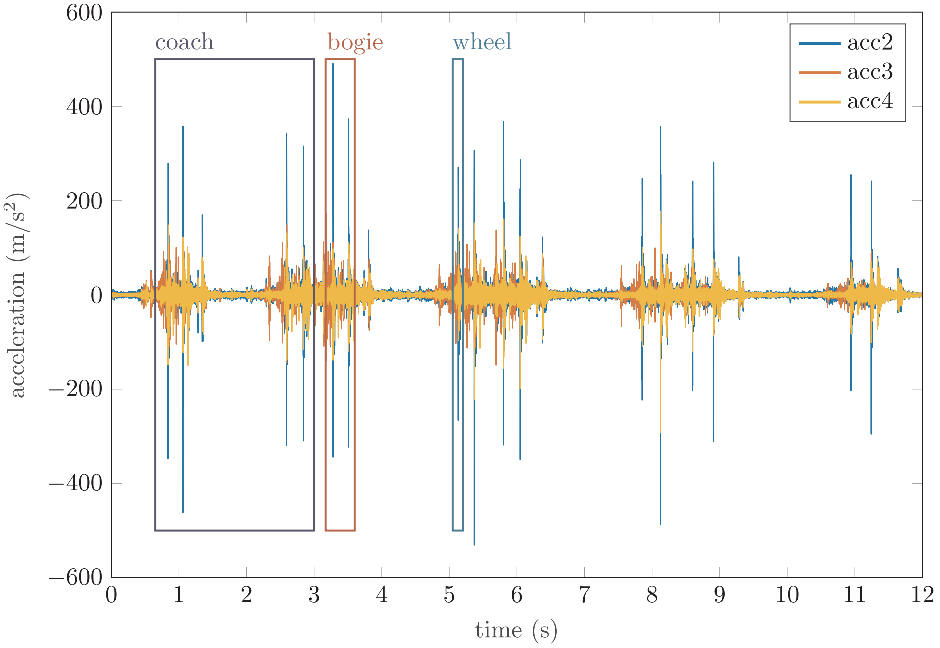

Fig. 3. Time history of the acceleration from a VIRM train with four coaches. The passage of the first coach, third bogie and seventh wheel are highlighted by a purple, red and green box, respectively. In addition to the wheel passages, more peaks can be identified. These are typically below ±200 m/s^2 and originate from the wheels running over irregularities (welds) in the vicinity of the crossing. (For interpretation of the references to colour in this figure legend, the reader is referred to the web version of this article.)

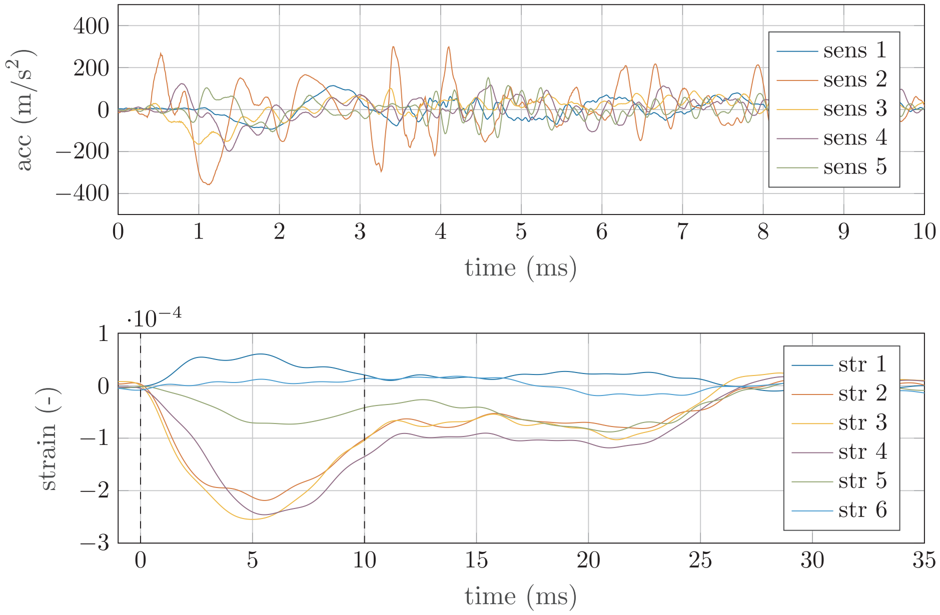

Fig. 4. Measured response of the frog caused by the passing of the tenth axle of a VIRM train. The top plot shows the response from the accelerometers, and the lower plot shows the measured strain. Note that the time axis is different for both plots. The time span of the top plot is indicated by the black lines in the bottom plot.

approximately 25 mm. It is expected that this peak is caused by a local surface imperfection.

From the strain response, it is found that sensor 1 measures a positive strain compared to the other strain gauges. This result means that this part of the frog shows a local extension compared to the compression for the other sensors. The signal from sensor 6 is very small and only shows a slight compression. This result is due to the orientation of this particular sensor, as it was practically not possible to install this sensor fully horizontal. The largest strain is measured by sensors 2, 3 and 4. The response of sensor 2 is smaller around t = 5 ms, but it has a similar magnitude after the 15 ms mark. For this time range, the largest strain is measured by sensor 4.

A close up of a passage of the first axle of an ICD train is shown in Fig. 5. This passage is measured on the same day as the result shown in Fig. 4.

The same observations can be made from Fig. 5 for the ICD train as were made for the VIRM train. The most notable differences are the increase in amplitude and the change in the response of strain gauge 4.

4.1. Displacement by time integration

As stated in Section 3, it can be valuable to know the displacement of the crossing. One option for obtaining this displacement is to use numerical time integration of the measured acceleration. Numerically, time integration is as simple as computing the cumulative sum multiplied by the time step; practically, this operation is not that simple.

One issue is obtaining the integration constants since the initial conditions are not known. To overcome this issue, the full time history is used in this case. Before the arrival of a train, both the initial velocity and position are assumed to be 0, i.e., the crossing is stationary in a reference position.

The larger issue with time integration is caused by the accumulation

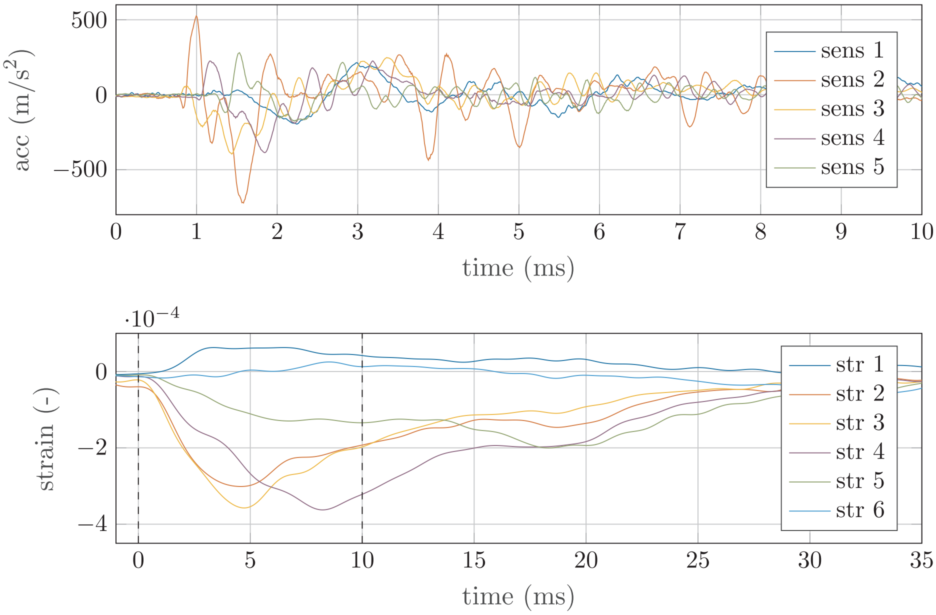

Fig. 5. Measured response of the frog caused by the passing of the first axle of an ICD train. The top plot shows the responses from the accelerometers, and the lower plot shows the measured strain. Note that the time axis is different for these plots. The time span of the top plot is indicated by the vertical black lines in the bottom plot.

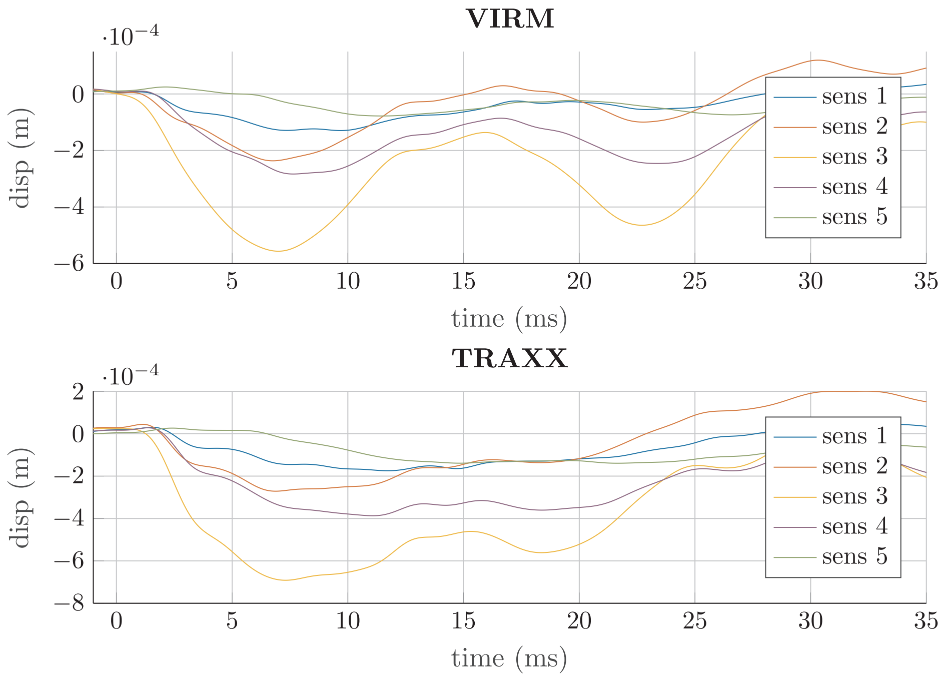

Fig. 6. Displacement of the crossing derived from the acceleration signals shown in Figs. 5 and 6.

of measurement noise, which causes a drift of the displacement. This noise can be reduced using a high-pass filter.

Similar to the filter used for the strain measurements, wavelet transformation is used to design the filter. The low cutoff frequency of the filter is obtained after an iterative search where the peak-peak displacement per wheel is maximized and the drift is minimized. The peak-peak displacement is defined as the difference between the minima that is caused by the passage of the axle and the proceeding maximum. Based on these criteria, a low cutoff frequency of 0.84 Hz is selected.

High-frequency content typically has a minor influence on the displacement, but to obtain a smoother result, a bandpass filter is used in this case. Similar to the strain measurements, the high cutoff frequency is set to 500 Hz. After filtering, the trapezoidal rule is used for time integration. To remove the remainder of the drift in the signal, the displacement is high-pass filtered again with the same low cutoff frequency of 0.84 Hz.

In Fig. 6, the displacements obtained from the accelerations already shown in Figs. 4 and 5 are presented.

The results presented in this figure should be treated as an accurate estimation and not as an absolute result, i.e., the maximum downward displacement is not limited to 0.7 mm, but it can be concluded that the total displacement of this crossing during the passing of an axle is in the range from 0.5 to 1.0 mm. Despite all the measures that were taken to reduce the drift, each response still had to be manually adjusted to be zero between $t = -5$ ms and $t = 0$ ms.

Accelerometer 2 measured the largest acceleration, but the largest displacement was obtained from accelerometer 3. The second largest displacement was obtained from accelerometer 4, which also shows a larger acceleration compared to accelerometer 3.

When the displacements are compared to the strain measurement in Figs. 4 and 5, it is observed that the displacements of accelerometers 3 and 4 have a similar trend and wavelength compared to strain gauge 4 up to approximately 15 ms. From the displacement, two minima can easily be identified; however, the second minimum is not clearly observable from the strain. Based on this result, it can be concluded that the strain is indeed related to the displacement of the crossing; however, the displacement does not always result in deformation of the strain gauges. The second minimum as found from the displacement is for instance most notably measured by strain gauge 5, which does not capture the first minimum very clearly.

4.2. Selection and comparison

Based on these findings, accelerometer 3 and strain gauge 4 are selected for a more in-depth comparison between the responses caused by the passage of the three different types of axles. The two measurements contain 44 axle passages: 16 from a VIRM train, 4 from a TRAXX locomotive and 24 from an ICR. Since not all axles can be presented in this paper, the axle passage that has the largest correlation for all passages of the same type will be presented. These axles were selected by the following procedure:

- A peak finder is used to detect the passage of the axles from strain gauge 3.
- Because peak finding is sensitive to noise, the cross covariance is computed to align the signals more accurately. The covariance is used in this case since this first subtracts the mean from the signal before the correlation is computed. This eliminates the influence of any offset.
- Time blocks around these instances are selected to represent the passage of the axles.
- Although the axle passages are aligned based on the strain, there was still a relative time shift for the acceleration signals of the different axles. Thus, the alignment of the passages is fine tuned using the cross correlation of the acceleration response. It is not possible to skip the previous step and apply the peak finder directly to the acceleration signal because there are more peaks than axles passages, as shown in Fig. 3.
- After the second alignment step, the cross correlation between each axle of the same type is computed for the response of accelerometer 3. In this case, the scaling from Eq. (1) is used.
- These correlation values are summed per axle, and for each type, the axle passage with the largest correlation value is selected. This is regarded as the most *average* response per axle type.

To ensure that this procedure is not influenced by the peak value of the axle passage, the following scaling factor is used when the cross

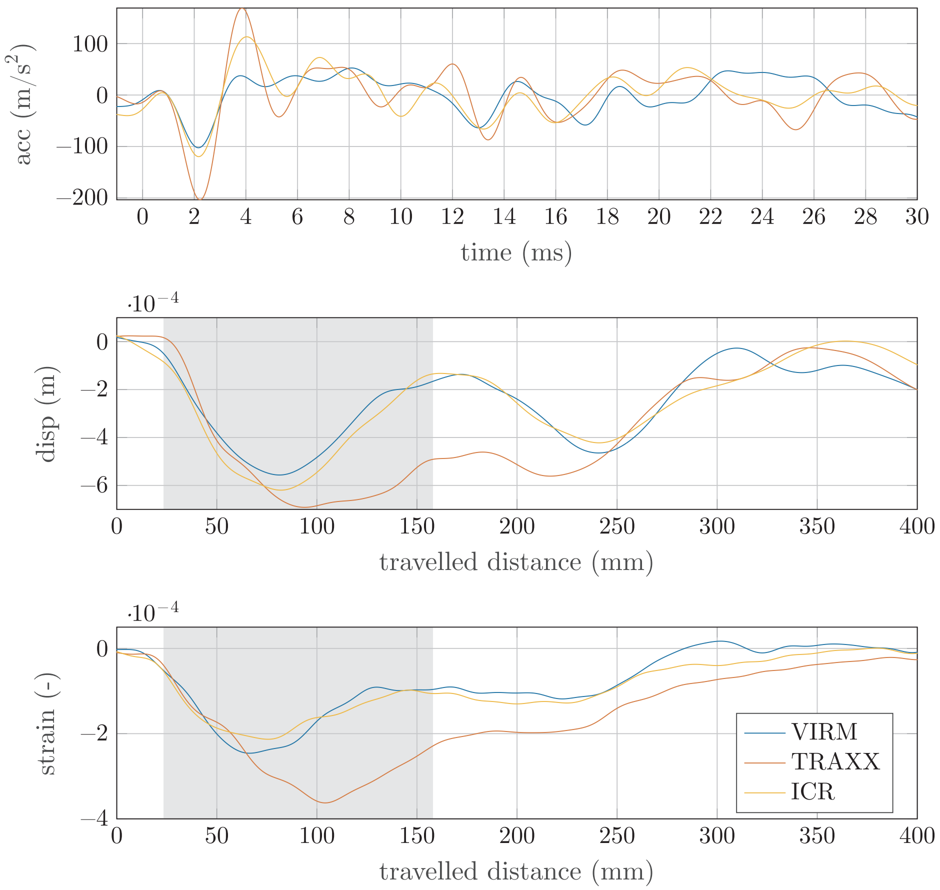

Fig. 7. Comparison of the responses from the passage of three different types of axles. The TRAXX and the ICR are the locomotive and the passenger coach of the ICD-type train, respectively. The top plot shows the filtered acceleration signal from accelerometer 3, the middle plot shows the displacement as obtained from the time integration of accelerometer 3, and the bottom plot shows the strain measured with strain gauge 4. Note that the x-axis is different for the lower two plots, where the time is multiplied by the velocity of the axle.

correlation is computed:

$$S_{xy,scaled}(\tau) = \frac{S_{xy}(\tau)}{\sqrt{S_{xx}(0)S_{yy}(0)}} \tag{1}$$

In this equation, $S_{xy}(\tau)$ is the cross correlation for a relative time shift τ, and $S_{xx}(0)$ is the auto correlation without a time shift. By using this scaling, the cross correlation will never be larger than 1. When the cross correlation is 1, the time histories of both signals are identical; however, the amplitudes of the signals can still be different.

For the VIRM train, the tenth axle is selected, as was already presented in Fig. 4. This is the trailing axle from a non-driven bogie; thus, it is typically the lightest axle of this type of train. For the TRAXX locomotive, the fourth axle is selected, as was already presented in Fig. 5. This is again a trailing axle and clearly from a driven bogie. For the ICR, the fifteenth axle is selected, which is a leading axle. The responses of these three axles are compared in Fig. 7.

In Fig. 7, three different responses are shown. In this figure, the response of strain gauge 4 is presented. This response is preferred compared to that from strain gauge 3 because the responses for the VIRM train were very similar for both sensors, whereas strain gauge 4 shows a different response for the TRAXX locomotive; thus, this sensor is expected to better highlight the difference between the different axles.

For both the strain and the displacement, the x-axis is transformed from time to travelled distance by multiplying the time by the velocity of each axle. This velocity is derived from the time between two axle passages of the same bogie and the axle spacing. To minimize errors, only the axles from the same bogie are used because they are closest together. The obtained velocities are 10.15, 11.1 and 11.2 m/s for the VIRM, TRAXX and ICR, respectively.

When the accelerations are compared for the different axles, the most notable difference is the absence of a significant positive peak for the VIRM train around t = 4 ms, but large peaks are found for the other two train types. Overall, these responses are quite similar, where the TRAXX locomotive shows the largest magnitude, and the response from the ICR wagon shows similarities with both the TRAXX and the VIRM.

For a more objective comparison between, the scaled cross correlation between these responses from t = 0 to t = 20 ms is computed. This comparison is presented in Table 3.

From this table, it is also clear that there is a better correlation between the accelerations from the TRAXX and the ICR as opposed to the VIRM and the other two types of axles.

When the displacements are compared, the TRAXX locomotive again shows the largest displacement; however, the peak value is only slightly larger compared to those of the ICR, which has a considerably lower axle load. The smallest magnitude is found for the VIRM, even though it has a higher axle load compared to the ICR wagon.

A wavelength of 135 mm is indicated by the light grey boxes in the lower two plots. Especially for the displacement, this length corresponds to the dominant wave in the response and extends along the travelling direction for two wavelengths. The displacement of the TRAXX locomotive is nearly stationary around the peak value, which might indicate a *bump-stop* behavior, for instance, caused by a ballast void.

For the strain measurements, the same wavelength is indicated. For the VIRM and ICR, the measured wavelength is slightly shorter than this

Table 3
Cross correlation values of the accelerations shown in Fig. 8 for the first 20 ms.

	VIRM	TRAXX	ICR
VIRM	1.0	0.72	0.74
TRAXX	0.72	1.0	0.87
ICR	0.74	0.87	1.0

box, whilst the wavelength of the TRAXX is slightly longer than this box. Most notably the peak value of the strain and the location of the peak value is different compared to the other two axle types. This is due to the increased axle load, as will be discussed in Section 5.2. Furthermore, as can be seen in Fig. 1, the strain gauges are situated before accelerometer 3, which can also be seen by the fact that the strain is already initiated before the gray area for all three axle types.

Based on this observation, it can be concluded that the strain and displacement exhibit similar wavelengths.

5. Analysis

The difference between the quantities that can be measured directly (acceleration and strain) are investigated in this section. In Section 5.1, wavelet analysis is used to highlight the differences in the acceleration signal, and the strain measurements are further analyzed in Section 5.2.

5.1. Wavelet analysis

To further analyze the acceleration signals, the wavelet spectra of the axle passages are analyzed. In this paper, the continuous wavelet transform based on the Fourier transform is used, and the Morlet wavelet is selected. The scales are distributed on a logarithmic scale.

The same axle passages as used for Fig. 7 are selected. To reduce the influence of measurement noise, the analysis is performed for averaged responses. Because there are always some differences between axle passages, even when they are from the same train, too much detail might be lost if the average of all passages is computed. Therefore, for the remainder of this subsection, the average of only three axle passages will be used.

For the VIRM train, next to the passage of the tenth axle, the passages of the seventh and ninth axles are also selected. For these axles, the correlations were found to be 0.9 and 0.96, respectively; thus, these responses are very similar. The wavelet coefficients for each axle are computed first, and then the complex values are averaged. The wavelet spectrum is shown in Fig. 8.

The top plot in Fig. 8 shows the absolute value of the wavelet coefficients. The red line in this spectrum indicates the high cutoff frequency of the filter designed in Section 4.1. In the lower plot, the time history obtained from the inverse transform of the complex coefficients is shown. The blue line represents the filtered signal, which contains all the information within the passband of the filter. The red line is the time signal that is removed by the filter, which can be regarded as the residual.

From this spectrum, it is clear that most energy is around 70 Hz and present between $t = 0$ and 25 ms. Given that the average speed of these axles is 10.25 m/s, 70 Hz corresponds to a wavelength of 146 mm, which was also found from the displacement in Fig. 7. After $t = 20$ ms, a second concentration of high energy is also notable around 100 Hz.

Around $t = 0$, a large negative peak in the time history is shown, which is caused by the transition of the train wheel from the stock rail onto the needle (the center part of the crossing). Around this transition, high-frequency content is found in the wavelet spectrum. There is a clear concentration of energy between 200 and 500 Hz, but energy is also visible for frequencies higher than 1 kHz.

Around $t = 10$ and 15 ms, two additional negative peaks are observed. From the wavelet spectrum, these peaks have similar frequency content compared to the initial peak, up to 500 Hz. The energy above 500 Hz is mainly present during the transition between $t = 0$ and 20 ms, where the magnitude of the residual is almost half the magnitude of the filtered signal. For the remainder of the time history, the residual is very small.

For the ICD, two distinct axle types are presented in Fig. 7. For each of these types of axles, the wavelet spectrum will be computed. Since the ICD train contains only a single TRAXX locomotive, the choice is limited to select other passages to compute the average spectrum. The first and second axles of this train had the highest correlations compared to the fourth axle, 0.69 and 0.86, respectively.

For the passenger coaches, there are 24 axles to choose from. The largest correlations were found for the seventh and eight axles: 0.97 and 0.94, respectively. Thus, these two responses are very similar to that of the fifteenth axle.

The same procedure as for the VIRM axles is followed, and the results are presented in Fig. 9. For comparison purposes, the color scale for both of these spectra and the spectrum presented in Fig. 8 is kept the same.

For the VIRM train, the frequency band around 70 Hz is the most dominant. These frequencies are also present in the spectra of the TRAXX and the ICR, but the frequencies have increased slightly. This increase can be related to the increase in velocity. The wavelength found for the VIRM was 146 mm, and the average speed of these axles is 11.15, resulting in a frequency of 76 Hz. From Fig. 9, the peak energy is found between 70 and 80 Hz for both spectra. Additionally, note that the duration is shorter, but the intensity is higher, both of which are related to the increased velocity.

For the VIRM train, a higher energy peak around 100 Hz was found between $t = 20$ and 25 ms. This peak is also found for both spectra from the ICD, although it is not as clear for the ICR as it is for the TRAXX. This frequency content appears to not be influenced by the velocity.

When the wavelet spectrum of the TRAXX is analyzed, a clear high-energy burst is found just after $t = 0$. This burst corresponds to the transition of the wheel because a peak is simultaneously found in the acceleration signal. The bandwidth of the peak below 500 Hz is comparable to that of the VIRM train as well as the duration. However, the intensity is much higher for the TRAXX. Furthermore, much higher frequencies are found with more energy. The most notable is the energy peak around 850 Hz, but reasonable magnitudes are found up to 3 kHz.

For the ICR, a similar behavior is found for the transition compared to the TRAXX. The energy content during this transition is higher for the ICR compared to the VIRM, and a peak is also found around 350 Hz.

For the VIRM train between $t = 10$ and 15 ms, an energy peak was found with a similar bandwidth compared to the transition. For both spectra in Fig. 9, a similar energy peak is found for the ICD, albeit with a smaller bandwidth. In particular, for the ICR, the energy is concentrated around 350 Hz. The time between the transition of the wheel and this energy peak appears to not be influenced by the velocity of the train.

When the residual time series are analyzed, a very similar response is found for both the TRAXX and the ICR. The magnitude is the same for both axle types but twice as large as the residual signal from the VIRM. From the wavelet spectrum, it is found that most of the energy of this residual is concentrated around 2.5 kHz.

Furthermore, it was found that the peak value of the measured acceleration was reduced by 50% for the ICR and 33% for the TRAXX and the VIRM passages. When only the lower frequency content is of interest, for instance when monitoring the settlement of the rail track, the dynamic range of the hardware can be optimized by using a suitable low-pass filter.

5.2. Strain signal

As mentioned in the introduction, the strain measurements were introduced to measure the surface waves in the crossing, but there is too much noise to measure this successfully in the field. However, the strain sensor can still provide valuable information. As was found in Fig. 7 and the description of the different trains in the introduction of this section, there is a relation between the axle load and the measured strain.

To further investigate this relation, the strain during the passage of all axles of the two trains used in this paper will be analyzed. First, the time axis is corrected using the speed of each bogie to express the strain as a function of the travelled distance, similar to Fig. 7. Because the variation in the velocity of the train is very small, this had a very minor

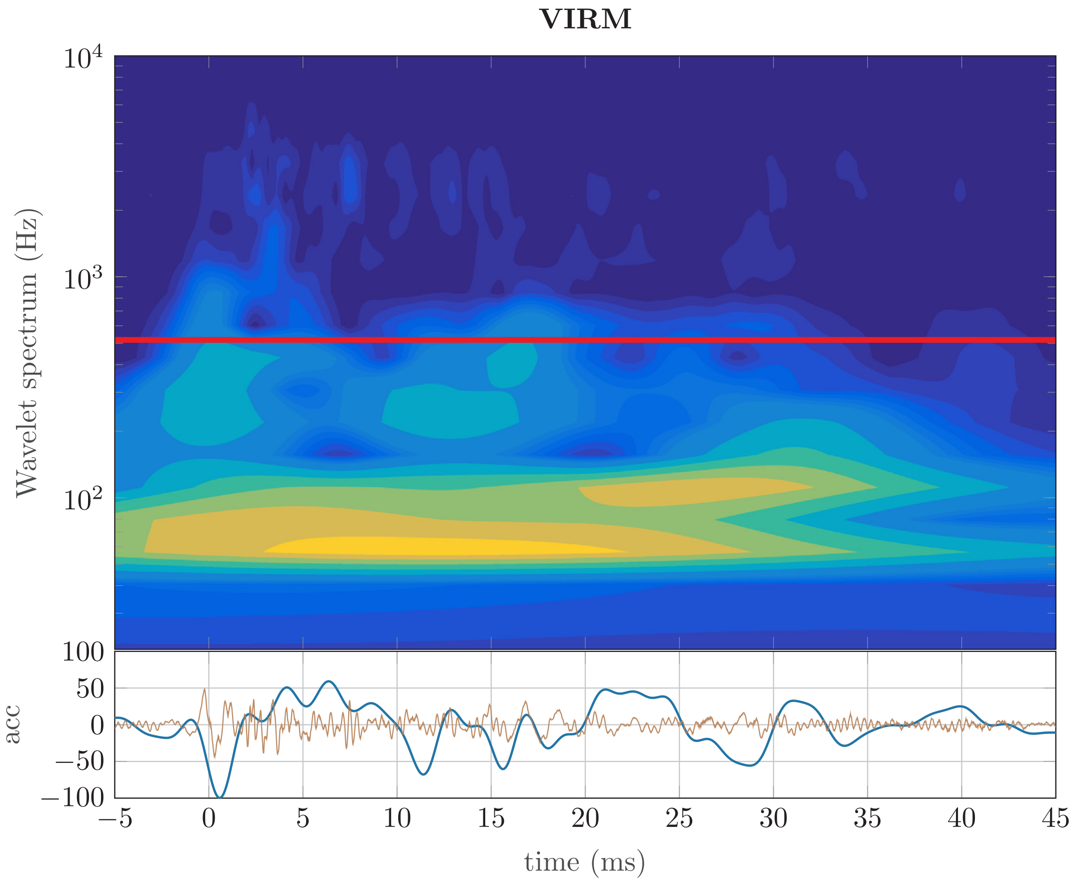

Fig. 8. Average wavelet response for the VIRM train. In the top plot, the average wavelet power spectrum is shown, where bright yellow represents high power and dark blue represents low power. The red line represents the cutoff frequency of the low-pass filter. In the lower plot, the inverse wavelet transform is shown. The blue line is the filtered response, and the red line is the residual. (For interpretation of the references to colour in this figure legend, the reader is referred to the web version of this article.)

influence, but it is believed to be a good practice for comparison purposes. Next, the signals are classified based on the axle load. For the ICD train, the first four axles belong to the TRAXX locomotive with a very high axle load, and the remaining axles belong to an ICR passenger coach with a low axle load. For the VIRM, this is slightly more complicated because it is an EMU. Because VIRM trains with only four coaches are symmetric, the first four and last four axles are labeled as driven, which indicates a higher axle load, and the eight axles in the middle are labeled as non-driven.

From each of these four sets, the mean value and the standard deviation are computed for each position of the wheel.

Before analyzing these data, note that the x-axes are not calibrated; thus, the results presented here are relative. There is no reference point for x = 0 mm, and the measurements are aligned based on the cross correlation before the mean and standard deviations are computed.

The axle load of the TRAXX locomotive is almost two times greater than the axle load of an ICR passenger coach. This result is also found from the peak amplitudes in the top plot of Fig. 10. The peak amplitude for the TRAXX is just above -4, whereas the peak amplitude for the ICR is just below -2. Furthermore, it is observed that the distance for the ICR to reach the maximum strain is considerably shorter and that the total distance is also shorter compared to TRAXX.

The VIRM train has a much smaller difference between the driven and non-driven coaches. The ratio for the axle load is almost 1.2, but the peak amplitude of the strain is equal for both the driven and the non-driven axles, as shown in the bottom plot of Fig. 10. The average axle load of a VIRM train is 15.5 tonnes, and a peak amplitude of just above -3 is found.

Although both responses from the VIRM train are based on the passage of eight axles, a considerably larger standard deviation is found for the driven axles. Based on the standard deviation, it is highly possible that there are driven axles with a smaller amplitude than non-driven axles, which also explains why the relation between peak strain and axle load was not clear when only individual passages were analyzed in Fig. 7.

Again, it was found that the response for the lighter axles is slightly shorter in distance compared to the heavier driven axles. The shaded areas of the standard deviation also overlap in this case; thus, it is not as clear as for the ICD train.

To further investigate the relation between the strain and the axle load, the peak values of the strain are plotted against the nominal axle load of the train. These are obtained the train maintenance company and represent typical values for these types of trains. There can still be some variation between the nominal and the actual axle load. The measurement points from both trains and a linear fit are shown in Fig. 11.

The coefficient for the linear fit was found to be $-1.8 \cdot 10^{-5}$ and norm of the residual is $28.5 \cdot 10^{-5}$. This figure also shows quite a large spread for the VIRM train, especially for the axles with higher axle load.

Although the strain measurements cannot be utilized as was initially intended, this result shows that strain gauges can provide valuable information. One can consider using these data with *weighing-in-motion* techniques to monitor the use of the crossing, but it might be even more valuable to use this technique to monitor the condition of the support for crossings. Because it is clearly related to the loading condition, high strain values can indicate that there is too much deformation that requires maintenance.

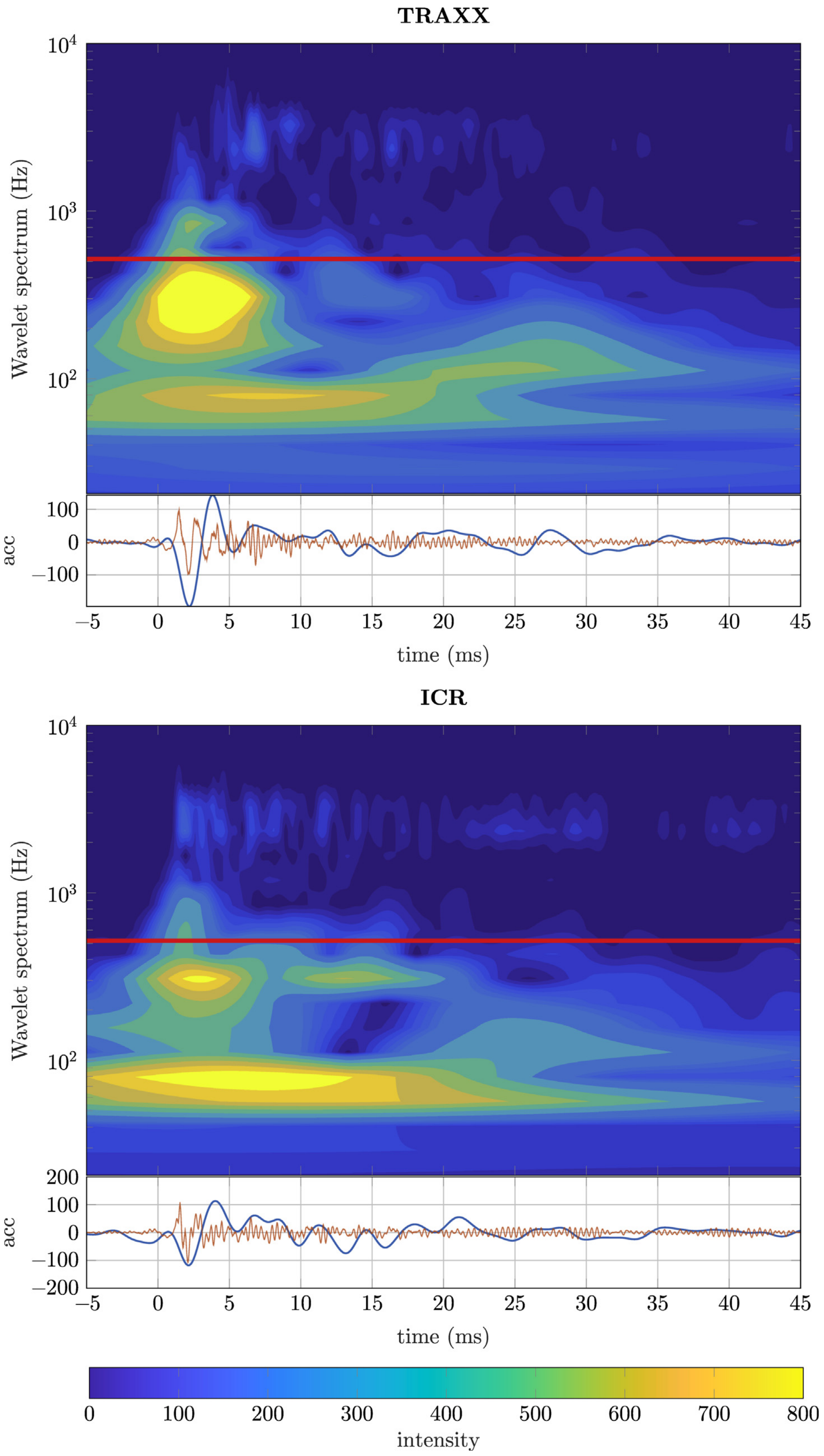

Fig. 9. Average wavelet response for the ICD train. This figure shows both the wavelet spectrum and the filtered time history with the residual of both types of axles. The cutoff frequency is again indicated with the red line. (For interpretation of the references to colour in this figure legend, the reader is referred to the web version of this article.)

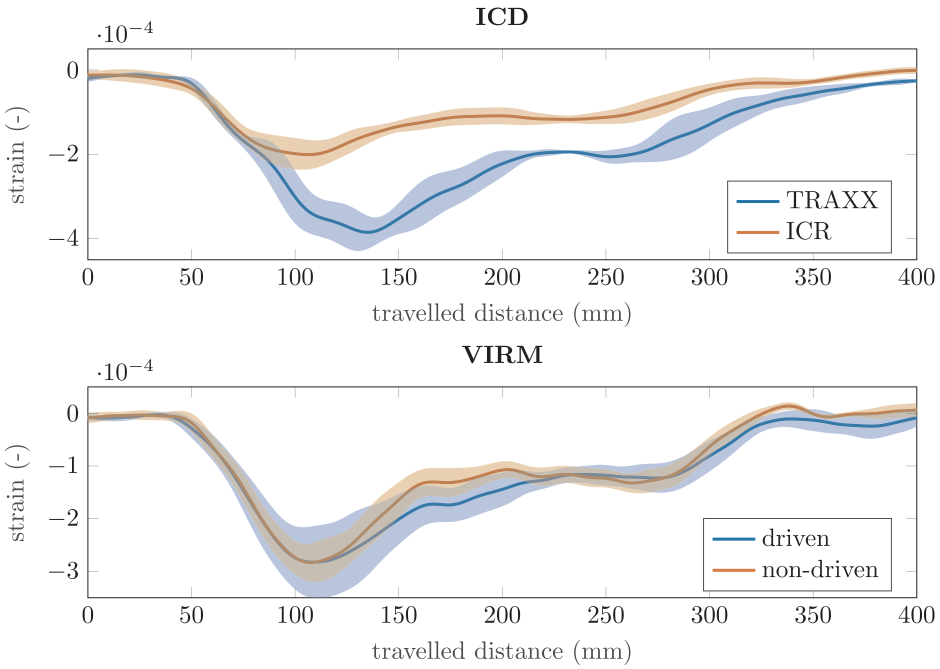

Fig. 10. Strain measurement of sensor 4 for four different types of axle passages. Both blue lines represent axles with a higher axle load, and the red lines are from axles that belong to passenger coaches with a lower axle load. The lines are the mean values of the measurement, and the shaded areas are the standard deviations. (For interpretation of the references to colour in this figure legend, the reader is referred to the web version of this article.)

6. Discussion and future work

As stated in Section 2, the aim of this paper is to investigate the dynamic response of a railway crossing based on dynamic measurements during normal operation. To highlight its use, the passages of two different train types are analyzed in detail, and in this section, the implications of the findings of this study will be discussed.

In Section 5.2, it is shown that strain gauges are very well suited for monitoring the loading condition. A clear relation between the axle load and the strain is found. Furthermore, it is found that the strain depends on the position of the axle; thus, it is best analyzed when adjusted for the speed of the axle. Strain gauges are inexpensive and well suited for monitoring purposes in the railway environment. Unfortunately, the signals of such gauges are very sensitive to noise; thus, signal conditioning should be performed as close as possible to the sensor.

The application of strain gauges is somewhat delicate, but given the cost of the sensor, strain gauges can already be installed during the fabrication of the railway components. Thus, when these components are installed in the field, only the datalogger needs to be connected, and the use of the component can be monitored. In [8], the sampling frequency for the strain was limited to 1 kHz, and from the results presented in Figs. 4 and 5, this sampling frequency appears to be sufficient. A relatively simple peak finding algorithm can be used to process the

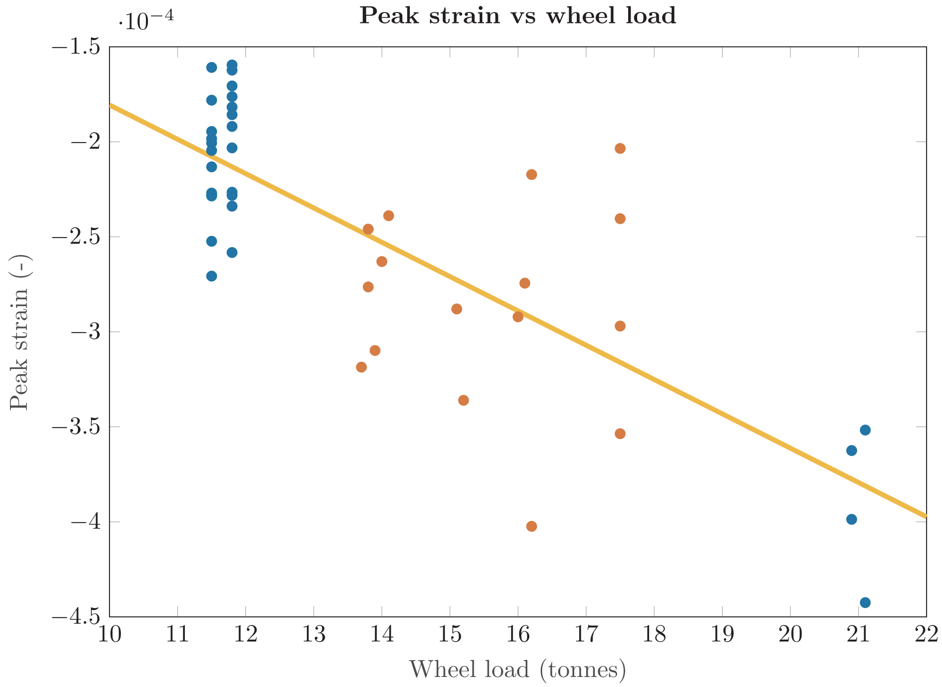

Fig. 11. Nominal axle load versus measure peak strain. The blue points are from the ICD train and the red points belong to the VIRM. The yellow line is a linear fit. (For interpretation of the references to colour in this figure legend, the reader is referred to the web version of this article.)

data to a manageable size for typical IoT networks.

Although this is a promising approach, it will take a long time before all track components are replaced with instrumented components, and optimization is still needed for the placement of the strain gauges on different components. However, measuring strain should not be overlooked when a measurement technique is needed to monitor support conditions.

Monitoring the accelerations of a crossing is also a reliable technique. In this case, industrial-grade accelerometers are used that feature IEPE signal conditioning. These accelerometers are very robust and reliable for use in harsh environments such as railways. These sensors are reasonably priced; however, data acquisition is slightly more complicated compared to strain gauges, mainly because higher sampling rates are required to fully capture the short wave vibrations caused by the transition of the train wheels. Field installation of accelerometers is considerably easier compared to strain gauges; thus, a monitoring system based on accelerometers can easily be retrofitted to rail components that are already installed in the field.

It is shown that the displacement can be obtained from the acceleration signal by using time integration, but this does require a well-tuned filter. For the case studied in this paper, a dominant wavelength of 135 mm is found for the displacement. The speed of the axles is limited to 11.2 m/s; thus, frequencies below 100 Hz can be related to the displacement. As was also found from the wavelet analysis in Section 5.1, the duration, intensity and center frequency of these waves are dependent on the train velocity.

The displacement obtained from time integration also shows a good correlation with the measured strain. This result highlights the benefits when both techniques are used together. Designing a bandpass filter to optimize time integration does require engineering judgment to evaluate the result. Using the strain as a reference will be very beneficial in this case. Further analysis is needed to investigate whether this filter also provides good results in other situations, such as for higher velocities.

The transition of the train wheel from the wing rail onto the needle causes a peak in the acceleration signal. Most of the energy of this transition is found between 200 and 500 Hz with a duration of almost 5 ms. For the ICD train, even higher frequency content is found for this transition. No relation between the intensity, duration or center frequency and the axle load or train speed has yet been found. Further analysis is needed in this area. Long-term monitoring of the accelerations in this frequency range is expected to provide information about the surface quality of the crossing and can indicate when reprofiling is needed.

In [8], a sample frequency of 5 kHz was used. Based on the frequency content found in Section 5.1 and the fact that a high-pass filter with a cutoff frequency at 500 Hz is used during most of the analyses presented here, this sampling frequency should be sufficient. However, frequency content above 3 kHz is also found, and if further analysis shows that this content contains valuable information, a higher sampling frequency of up to 10 kHz may be needed. Using such high sampling frequencies renders monitoring the accelerations less suitable for data transfer over IoT networks. Thus, with further research, an algorithm needs to be defined that processes the raw data to a more manageable size.

7. Conclusion

In this paper, an extensive method to measure the dynamics of a frog is presented using accelerometers and strain gauges. The responses of both measurement techniques are analyzed for two different train types. It was found that each of these techniques has its own benefits and is capable of highlighting different features of different loading conditions.

From the strain measurements, a good relationship between the strain and axle load is found; thus, this technique is very well suited for monitoring the support condition of rail components.

More detail is found from the acceleration signal. By using time integration, an estimate of the displacement can be made. For the crossing monitored in this work, a dominant wavelength of 145 mm is found. With the speed of a train limited to 11.2 m/s, this corresponds to frequencies of up to 80 Hz.

Higher frequency content is also found. During the transition of the wheel from the wing rail onto the needle, an energy peak between 200 and 500 Hz is found. For the ICD train, high-energy peaks were also found up to 1 kHz. These accelerations are related to transient wheel-rail contact.

Acknowledgment

This research is part of the STW/ProRail project (Detection and Diagnosis of Railway Track Short Wave Anomalies, DrTrack), project 12246, which is partly funded by the Ministry of Economic Affairs of the Netherlands.

References

[1] M. Molodova, Z. Li, R. Dollevoet, Axle box acceleration: measurement and simulation for detection of short track defects, Wear 271 (1-2) (2011) 349–356, http://dx.doi.org/10.1016/j.wear.2010.10.003 ISSN 0043-1648.

[2] P. Salvador, V. Naranjo, R. Insa, P. Teixeira, Axlebox accelerations: their acquisition and time-frequency characterisation for railway track monitoring purposes, Measurement 82 (Supplement C) (2016) 301–312, http://dx.doi.org/10.1016/j.measurement.2016.01.012 ISSN 0263-2241.

[3] K. Knothe, S. Grassie, Modelling of railway track and vehicle/track interaction at high frequencies, Vehic. Syst. Dynam. 22 (3-4) (1993) 209–262, http://dx.doi.org/10.1080/00423119308969027.

[4] M. Pletz, W. Daves, H. Ossberger, A wheel set/crossing model regarding impact, sliding and deformation-explicit finite element approach, Wear 294-295 (0) (2012) 446–456, http://dx.doi.org/10.1016/j.wear.2012.07.033 ISSN 0043-1648.

[5] A. Johansson, B. Palsson, M. Ekh, J. Nielsen, M. Ander, J. Brouzoulis, E. Kassa, Simulation of wheel-rail contact and damage in switches & crossings, Wear 271 (1–2) (2011) 472–481, http://dx.doi.org/10.1016/j.wear.2010.10.014 ISSN 0043-1648, Proceedings of the 8th International Conference on Contact Mechanics and Wear of Rail/ Wheel Systems, Florence, 2009..

[6] D. Barke, W.K. Chiu, Structural health monitoring in the railway industry: a review, Struct. Health Monitor. 4 (1) (2005) 81–93, http://dx.doi.org/10.1177/1475921705049764.

[7] G. Kouroussis, C. Caucheteur, D. Kinet, G. Alexandrou, O. Verlinden, V. Moeyaert, Review of trackside monitoring solutions: from strain gages to optical fibre sensors, Sensors 15 (8) (2015) 20115–20139, http://dx.doi.org/10.3390/s150820115 ISSN 1424-8220.

[8] Liu Chong, Wei Jiahong, Zhang Zhixin, Liang Junsheng, Ren Tongqun, Xu Hongquan, Design and evaluation of a remote measurement system for the online monitoring of rail vibration signals, Proc. Inst. Mech. Eng., Part F: J. Rail Rapid Transit 230 (3) (2016) 724–733, http://dx.doi.org/10.1177/0954409714560421.

[9] E. Kassa, J. Nielsen, Dynamic interaction between train and railway turnout: full-scale field test and validation of simulation models, Vehicle Syst. Dynam. 46 (sup1) (2008) 521–534, http://dx.doi.org/10.1080/00423110801993144.

[10] D. Nicklisch, J. Nielsen, M. Ekh, A. Johansson, B. Pålsson, J. Reinecke, A. Zoll, Simulation of wheel-rail contact forces and subsequent material degradation in switches & crossings, in: Proceedings 21st International Symposium on Dynamics of Vehicles on Roads and Tracks, Stockholm, 2009.

[11] S. Bruni, I. Anastasopoulos, S. Alfi, A.V. Leuven, G. Gazetas, Effects of train impacts on urban turnouts: modelling and validation through measurements, J. Sound Vib. 324 (3-5) (2009) 666–689, http://dx.doi.org/10.1016/j.jsv.2009.02.016 ISSN 0022-460X.

[12] WITT IndustrieElektronik GmbH, Automated Point Inspection, URL < http://en.witt-solutions.de/assets/API_ESAH-M_Datasheet.pdf >, 2016.

[13] Y. Tsai, H. Kolsky, A study of the fractures produced in glass blocks by impact, J. Mech. Phys. Solids 15 (4) (1967) 263–278.